University Library

MINERVA ACCESS

A gateway to Melbourne's research publications

Minerva Access is the Institutional Repository of The University of Melbourne

Author/s:
Broadway, DA;Scholten, SC;Tan, C;Dontschuk, N;Lillie, SE;Johnson, BC;Zheng, G;Wang, Z;Oganov, AR;Tian, S;Li, C;Lei, H;Wang, L;Hollenberg, LCL;Tetienne, J-P

Title:
Imaging Domain Reversal in an Ultrathin Van der Waals Ferromagnet

Date:
2020-10-01

Citation:
Broadway, D. A., Scholten, S. C., Tan, C., Dontschuk, N., Lillie, S. E., Johnson, B. C., Zheng, G., Wang, Z., Oganov, A. R., Tian, S., Li, C., Lei, H., Wang, L., Hollenberg, L. C. L. & Tetienne, J. -P. (2020). Imaging Domain Reversal in an Ultrathin Van der Waals Ferromagnet. Advanced Materials, 32 (39), https://doi.org/10.1002/adma.202003314.

Persistent Link:
https://hdl.handle.net/11343/271003

Imaging domain reversal in an ultrathin van der Waals ferromagnet

David A. Broadway,[1,2,3,*] Sam C. Scholten,[1,2,*] Cheng Tan,[4,*] Nikolai Dontschuk,[1,2] Scott E. Lillie,[1,2] Brett C. Johnson,[1,2] Guolin Zheng,[4] Zhenhai Wang,[5,6] Artem R. Oganov,[5,7,8] Shangjie Tian,[9] Chenghe Li,[9] Hechang Lei,[9,†] Lan Wang,[4,‡] Lloyd C. L. Hollenberg,[1,2,§] and Jean-Philippe Tetienne[1,2,¶]

[1]*School of Physics, University of Melbourne, Parkville, VIC 3010, Australia*

[2]*Centre for Quantum Computation and Communication Technology, School of Physics, University of Melbourne, Parkville, VIC 3010, Australia*

[3]*Current address: Department of Physics, University of Basel, Klingelbergstrasse 82, Basel CH-4056, Switzerland*

[4]*School of Science, RMIT University, Melbourne, VIC 3000, Australia*

[5]*Skolkovo Institute of Science and Technology, Skolkovo Innovation Center, 3 Nobel Street, Moscow 143026, Russia*

[6]*School of Telecommunication and Information Engineering, Nanjing University of Posts and Telecommunications, Nanjing, Jiangsu 210003, China*

[7]*Moscow Institute of Physics and Technology, 9 Institutsky Lane, Dolgoprudny, Moscow Region 141700, Russia*

[8]*International Center for Materials Discovery, Northwestern Polytechnical University, Xi'an 710072, China*

[9]*Department of Physics and Beijing Key Laboratory of Optoelectronic Functional Materials & Micro-Nano Devices, Renmin University of China, 100872 Beijing, China*

Author Manuscript

This is the author manuscript accepted for publication and has undergone full peer review but has not been through the copyediting, typesetting, pagination and proofreading process, which may lead to differences between this version and the Version of Record. Please cite this article as doi: 10.1002/adma.202003314

This article is protected by copyright. All rights reserved.

Author Manuscript

Abstract

The recent isolation of two-dimensional van der Waals magnetic materials has uncovered rich physics that often differs from the magnetic behavior of their bulk counterparts. However, the microscopic details of fundamental processes such as the initial magnetization or domain reversal, which govern the magnetic hysteresis, remain largely unknown in the ultrathin limit. Here we employ a widefield nitrogen-vacancy (NV) microscope to directly image these processes in few-layer flakes of magnetic semiconductor vanadium triiodide (VI_3). We observe complete and abrupt switching of most flakes at fields $H_c \approx 0.5 - 1$ T (at 5 K) independent of thickness down to two atomic layers, with no intermediate partially-reversed state. The coercive field decreases as the temperature approaches the Curie temperature ($T_c \approx 50$ K), however, the switching remains abrupt. We then image the initial magnetization process, which reveals thickness-dependent domain wall depinning fields well below H_c. These results point to ultrathin VI_3 being a nucleation-type hard ferromagnet, where the coercive field is set by the anisotropy-limited domain wall nucleation field. This work illustrates the power of widefield NV microscopy to investigate magnetization processes in van der Waals ferromagnets, which could be used to elucidate the origin of the hard ferromagnetic properties of other materials and explore field- and current-driven domain wall dynamics.

Keywords: van der Waals materials, 2D magnetism, vanadium triiodide, nitrogen-vacancy center, magnetic imaging, magnetic domains

* These authors contributed equally to this work.

† hlei@ruc.edu.cn

‡ lan.wang@rmit.edu.au

§ lloydch@unimelb.edu.au

¶ jtetienne@unimelb.edu.au

This article is protected by copyright. All rights reserved.

Author Manuscript

Two-dimensional (2D) van der Waals materials exhibiting intrinsic magnetic order have attracted enormous interest in the last few years.[1–5] However, despite much progress in the control of their magnetic properties, for example through electrostatic gating or control of the stacking order,[6–9] little is known about the mechanisms governing fundamental magnetic processes in the ultrathin limit. For instance, the extensively studied materials CrI_3 (a semiconductor) and Fe_2GeTe_3 (a metal) are soft ferromagnets in the bulk crystal form with a remanent magnetization far below the saturation magnetization (a few percent),[10,11] but surprisingly they become hard ferromagnets when exfoliated to a few atomic layers, with a near square-shaped hysteresis and a large coercive field of $H_c \sim 0.1 - 1$ T.[1,12–14] Since hard ferromagnetic properties are crucial to applications, especially as a building block for van der Waals magnetic heterostructures, it is of paramount importance to understand the mechanisms that govern magnetization reversal in these systems. Unfortunately, the heterogeneous nature of exfoliated van der Waals samples precludes performing the macroscopic magnetization measurements that are normally employed to analyze bulk magnets, calling for the development of innovative approaches.

We address this problem by directly imaging the evolution of the magnetization of ultrathin flakes using a widefield nitrogen-vacancy (NV) microscope. This recently developed magnetic imaging tool[15–18] is particularly well suited to the rapid analysis of multiple micrometer-sized samples such as exfoliated van der Waals materials, and allows us to track the domain structure of individual flakes with sub-micron spatial resolution. This widefield approach contrasts with single NV scanning magnetometry,[19–21] which offers a better spatial resolution ($\sim$ 50 nm) but is inherently slow and limited to small image sizes. Compared with magneto-optical imaging techniques, which are the gold standard for spatially-resolved studies of 2D magnets,[1,2] widefield NV imaging features a similar spatial resolution ($\sim$ 500 nm, limited by optical diffraction) but presents the advantage of being quantitative, enabling the absolute magnetization of individual flakes to be determined.

Our widefield NV microscope employs a diamond substrate incorporating a near-surface layer of magnetically sensitive NV centers (Figure 1a). The diamond surface is patterned with a metallic grid to facilitate the localization of the flakes which are prepared directly on top of the grid (see Figure S1, grid not shown in Figure 1a for clarity). The distance between the flakes and the NV layer is about 300 nm, such that it does not limit the sensitivity or spatial resolution.[22] The NV layer is excited by a laser and its photoluminescence is imaged

This article is protected by copyright. All rights reserved.

Author Manuscript

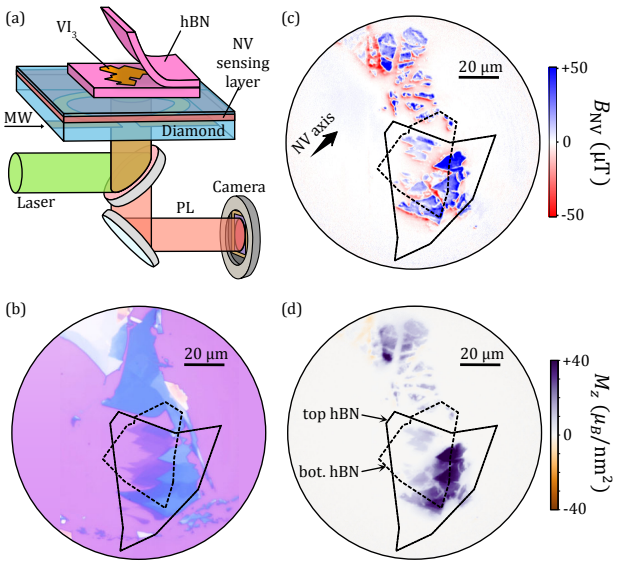


FIG. 1. **Widefield NV imaging of ultrathin van der Waals magnets.** (a) Schematic of the widefield NV microscope, comprising an NV-diamond sensing chip on which the hBN/VI_3 heterostructures are prepared. PL: photoluminescence; MW: microwaves. (b) Optical micrograph of exfoliated VI_3 flakes (sample #1) on a Si substrate prior to encapsulation and transfer to the diamond. (c) NV magnetic field map (B_{NV}) of the flakes seen in (b) after transfer to the diamond, at 5 K. The NV projection axis is indicated by the thick arrow and points partly out of the plane. A bias field of $B_{NV}^{bias} = 5$ mT was applied along the NV axis during the measurement, which was subtracted in the plotted map. (d) Map of the out-of-plane magnetization (M_z) deduced from (c). In (b-d), the dashed lines indicate the location of the hBN top and bottom layers.

on a camera. The metallic grid also serves to prevent the laser light from reaching the sample. Magnetic imaging is realized by sweeping the frequency of an applied microwave field to obtain an optically-detected magnetic resonance (ODMR) spectrum.[23–25] The ODMR spectrum, acquired under a small bias field $B_{NV}^{bias} = 5$ mT aligned with the symmetry axis of a given family of NV centers, exhibits two electron spin resonances separated by a Zeeman splitting $\Delta f = 2\gamma_{NV}(B_{NV}^{bias} + B_{NV})$ where B_{NV} ($\ll B_{NV}^{bias}$) is the stray field generated by the sample, projected along the NV axis, and $\gamma_{NV} = 28.035(3)$ GHz/T is the NV gyromagnetic ratio[23,24] (see example ODMR spectrum in Figure S7). Each pixel of the camera records an ODMR spectrum, allowing a B_{NV} map of the sample to be generated. The diamond-sample assembly is placed in a cryostat allowing measurements from 4-300 K.[26]

We studied ultrathin samples of magnetic semiconductor vanadium triiodide (VI_3). The

This article is protected by copyright. All rights reserved.

Author Manuscript

magnetic properties of this van der Waals material were recently analyzed in the bulk form, [27–29] reporting a hard ferromagnetic behavior with an out-of-plane anisotropy and a high coercive field at low temperatures, $H_c \approx 1$ T. Flakes mechanically exfoliated from a bulk VI_3 crystal were encapsulated with hexagonal boron nitride (hBN) to prevent degradation, and transferred to the diamond substrate. Figure 1b shows the optical image of a VI_3 sample on a Si substrate (prior to transfer), comprising flakes of various thicknesses from tens of nanometers down to three atomic layers in this case (based on the optical contrast, see below). The NV magnetic field image (B_{NV}) of the same sample after transfer and cooling to a temperature of 5 K is shown in Figure 1c, revealing magnetic signals of tens of microteslas. Knowing the projection axis of the measurement and the direction of the magnetization in the sample (out-of-plane, z axis), we can reconstruct the magnetization map (M_z),[21] shown in Figure 1d. The magnetization is given per unit surface area and reaches 50 μ_B/nm^2 for the thickest flakes in this sample (≈ 20 nm). Interestingly, the widefield image in Figure 1d allows us to directly compare samples fully encapsulated with hBN to samples with hBN on one side only or with no hBN at all. We find that the VI_3 flakes that are not covered by hBN (top of the images) are still magnetic but appear fragmented with a reduced magnetization as a result of a short exposure to air during loading (≈ 5 minutes). However, there is no visible effect of the hBN underlayer and no discontinuity in M_z for flakes overlapping an hBN edge. This indicates that the magnetic properties of the flakes imaged are not measurably affected by interactions with the substrate. We also performed measurements under a larger bias field ($B_{\mathrm{NV}}^{\mathrm{bias}} = 200$ mT instead of 5 mT) returning a very similar M_z map (see Figure S15). Therefore, for consistency all the measurements shown in the paper were taken at 5 mT.

To investigate the properties of ultrathin VI_3, we prepared several few-layer samples (fully encapsulated with hBN) and imaged their magnetization in similar conditions. Prior to imaging, a magnetic field $B_z = +1$ T was applied in the $+z$ direction to remove the domain structure. Optical contrast maps of four samples studied are shown in Figure 2a, from which the thickness of each flake was inferred (see Supporting Information, section III), and are compared to the corresponding magnetization maps (Figure 2b). Most flakes down to 3 layers, as well as one bilayer flake in sample #4, show a clear magnetic signal, demonstrating that VI_3 remains ferromagnetic down to two atomic layers. The variations in magnetization within a given flake are attributed to local imperfections arising from the encapsulation process (see Figure S2-S5) and/or degradation due to residual oxygen or

This article is protected by copyright. All rights reserved.

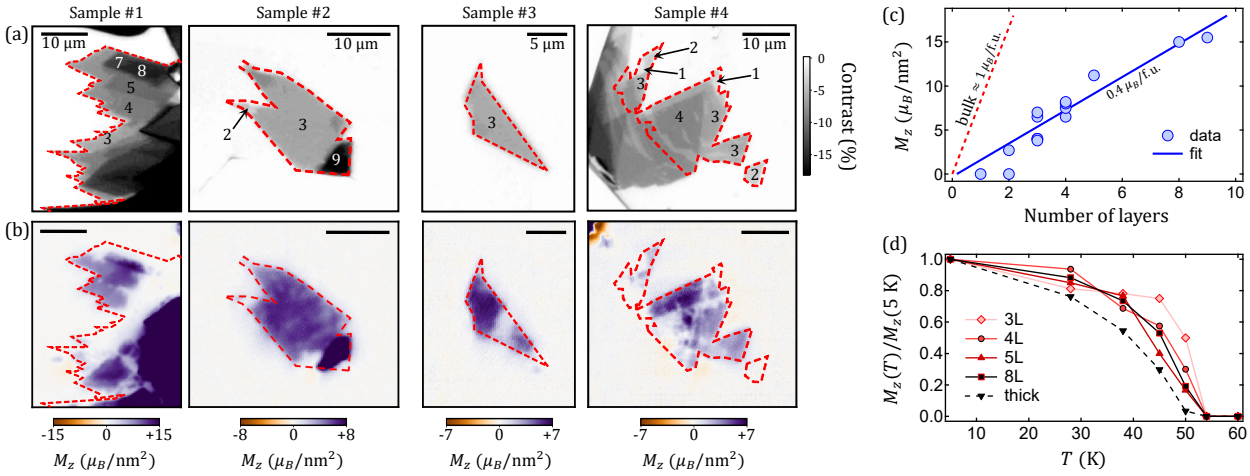


FIG. 2. **Magnetization maps of few-layer VI_3 flakes.** (a) Optical contrast maps of four different samples prior to transfer to the diamond. The contrast is defined from the red channel intensity, relative to the substrate. The numbers indicate the number of atomic layers inferred from the optical contrast, corroborated by atomic force microscopy measurements (see Supporting Information, section III). The red dashed boxes indicate the flakes that were effectively transferred to the diamond (see Supporting Information, section II). (b) Corresponding magnetization maps at 5 K. (c) Maximum M_z value extracted from (b) for a selection of flakes, as a function of thickness. The blue line is a fit to the data points, excluding the flakes showing zero magnetization. The red dashed line corresponds to the bulk spontaneous magnetization of about one Bohr magneton per formula unit (1 μ_B/f.u.) or 5 μ_B/nm^2 per layer.[28,29] (d) Magnetization as a function of temperature for several flakes in sample #1, with thickness from 3 layers ('3L') up to ≈ 20 nm ('thick').

water in the environment. Sample degradation is also the likely explanation for the absence of magnetic signal in some regions, including monolayer and bilayer regions in sample #4 but also thicker regions (3-4 layers) in all samples. We did not detect any magnetic signal from monolayer flakes, but this could simply be due to degradation rather than an intrinsic property. Monolayer flakes were found to be very difficult to fabricate and identify given the low optical contrast (2%, see Figure S6), preventing a more systematic study. Nevertheless, the magnetic sensitivity of our measurements should in principle be sufficient to detect a magnetic monolayer, as illustrated by the large signal-to-noise ratio of bilayer and trilayer flakes in Figure 2b.

This article is protected by copyright. All rights reserved.

Author Manuscript

Author Manuscript

The spontaneous (areal) magnetization is estimated by taking the maximum M_z value observed in the images for each domain observed. This is plotted as a function of thickness up to 9 layers in Figure 2c, revealing a roughly linear relationship with a slope of 1.9(2) μ_B/nm^2 per atomic layer, which amounts to about 0.4 μ_B per formula unit (μ_B/f.u). This is somewhat lower than the spontaneous magnetization of ≈ 1 μ_B/f.u. measured for bulk VI_3 crystals, [28,29] again possibly due to degradation of our ultrathin VI_3 samples. Another possible explanation is a mixture of ferromagnetic and antiferromagnetic interlayer couplings on a sub-micron scale. This would give a reduction in average magnetization and only a subtle difference between an odd and even number of layers, which cannot be ruled out by our data. Interestingly, our ab initio calculations predict that the antiferromagnetic state is energetically favorable in bilayer and trilayer VI_3 (see Supporting Information, section XIII), lending credibility to this interpretation.

By recording magnetic field images at various temperatures T (see Figure S10), it is possible to determine the $M_z - T$ relationship as a function of thickness. This is shown in Figure 2d, which reveals a Curie temperature of $T_c \approx 50$ K similar for all the flakes analyzed (down to 3 layers in this case), in agreement with the T_c of bulk VI_3.[27–29] The magnetization of the thickest flakes (20 nm) tends to drop more rapidly than for thinner flakes, which we attribute to domain formation in this small applied magnetic field.

In hard magnetic materials, the switching process is governed by either the nucleation or pinning of domain walls.[30] In bulk magnets, these two mechanisms are normally distinguished by their initial magnetization curves. The domain walls move freely in a nucleation-type magnet, which has a high initial susceptibility, while they are constantly being trapped in a pinning-type magnet, so the initial susceptibility is small until the depinning field is reached. To determine the limiting mechanism in ultrathin VI_3, we applied pulses (~ 10 s duration) of magnetic field in the $-z$ direction to samples initially magnetized in the $+z$ direction, before returning to a low field ($B_{\mathrm{NV}}^{\mathrm{bias}} = 5$ mT) such that imaging was in the optimum magnetic field range for ODMR. Series of images after pulses of increasing amplitude up to -1 T are shown in Figure 3a and 3b for samples #1 and #4, respectively (see additional data in Figure S12). The magnetization is observed to reverse abruptly, that is, regions of contiguous material switch sign completely at once rather than creating partially reversed domains. This is the signature of a nucleation-type magnet. The switching field, which corresponds to the coercive field H_c in this case, lies in the range $0.5 - 1$ T for most

This article is protected by copyright. All rights reserved.

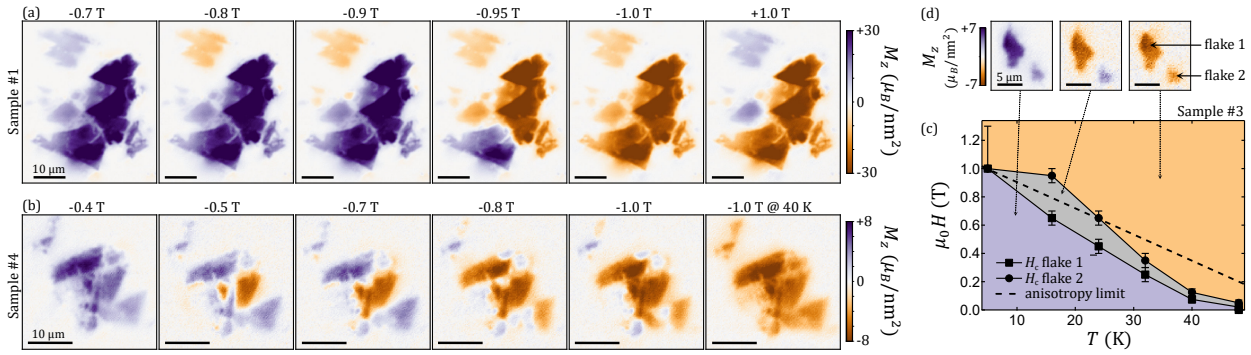


FIG. 3. **Imaging domain reversal in few-layer VI_3 flakes.** (a) M_z maps of sample #1 for increasing magnetic field pulse amplitude from -0.7 T to -1.0 T (from left to right) applied along the $-z$ direction (pulse duration ~ 10 s excluding rise/fall times), starting with the flakes magnetized in the $+z$ direction. In the last image of the series, a $+1.0$ T pulse was applied to reverse the magnetization back to its original sign. (b) M_z maps of sample #4 after pulse amplitudes from -0.4 T to -1.0 T. In the last image of the series, a -1.0 T pulse was applied while heating the sample to $T = 40$ K to facilitate magnetization reversal. All images in (a,b) were acquired under a small bias field $B_{\mathrm{NV}}^{\mathrm{bias}} = 5$ mT. (c) $H - T$ phase diagram of the magnetic state of two flakes in sample #3 constructed from image series similar to those in (a,b) at various temperatures (see Figure S11). The data points indicate the coercive field H_c for each flake. The error bars correspond to the step size in the field amplitude. The large error bar on the lowest temperature points denotes the fact only a lower bound for H_c is determined in this case. The dashed line is the Stoner-Wohlfarth model for the coercive field [30] using the temperature-dependent anisotropy constant measured for bulk VI_3 in Reference [31]. The purple (orange) shaded region corresponds to the two flakes magnetized in the $+z$ ($-z$) direction, while in the grey region only the largest flake has switched. (d) Example M_z maps corresponding to each magnetic state, recorded at 5 K.

flakes, with no apparent correlation with flake thickness. The bilayer flake in sample #4, for instance, lies in the middle of this range, with a coercive field of $0.7 - 0.8$ T. Some flakes have an even larger coercive field, as evidenced by the purple domains remaining in sample #4 after applying -1.0 T (which is the maximum field amplitude we can apply in our setup), or by the orange domains in sample #1 after applying $+1.0$ T. The variation in H_c between different flakes is attributed to shape irregularities or defects that can locally lower the nucleation field compared to the maximum value (which is related to the anisotropy

This article is protected by copyright. All rights reserved.

Author Manuscript

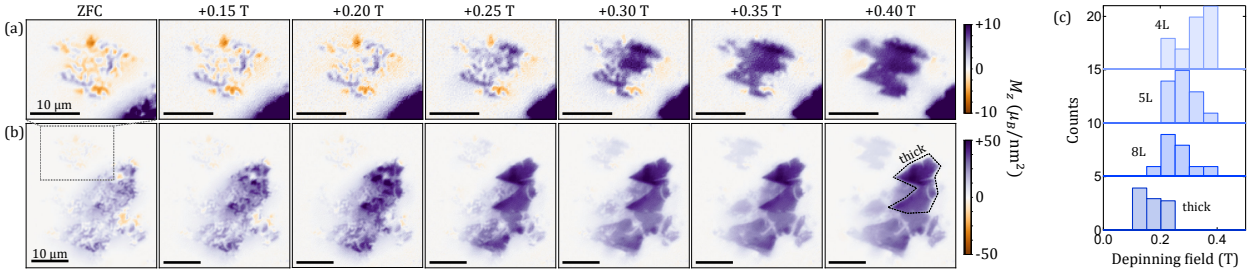


FIG. 4. **Imaging the initial magnetization of few-layer VI_3 flakes.** (a,b) M_z maps of sample #1 as a function of the magnetic field pulse amplitude starting from the virgin state (zero-field cooling, ZFC). (a) is a magnified version of (b) highlighting the region containing flakes from 4 to 8 layer thick. (c) Histograms of the number of domain wall jumps versus magnetic field for flakes of different thickness, constructed from (a) for the thin flakes (4L, 5L, 8L) and from (b) for thick flakes (10-20 nm thickness, dashed box).

constant, as discussed below).

By heating the sample to 40 K during the application of the pulse, we were able to switch all of the flakes as shown in Figure 3b (last image of the series), suggesting that the coercive field decreases with increasing temperature. Repeating the magnetic field sweep at different temperatures (see full image series in Figure S11) allows us to form a phase diagram from which the $H_c - T$ relation can be identified. This is shown in Figure 3c for two flakes in sample #3, with example M_z maps in the different states shown in Figure 3d. For both flakes, H_c decreases monotonically from 1 T to zero when T is increased from 5 K to 50 K. The values are in broad agreement with the Stoner-Wohlfarth model [30] (dashed line in Figure 3c) in which the coercive field is only limited by the strength of the perpendicular anisotropy (see details in Supporting Information, section IX). We note that the effective anisotropy constant used in this model includes the demagnetising contribution accounting for shape anisotropy. These results indicate that the coercivity of ultrathin VI_3 is mostly governed by anisotropy-limited domain wall nucleation processes, and hence that magnetization reversal occurs in a near-coherent regime.

To confirm this picture, we directly image the initial magnetization starting from the virgin state, as shown in Figure 4a and 4b for sample #1 (see additional data in Figure S13). The multi-domain structure visible after zero-field cooling progressively disappears when magnetic field pulses of increasing amplitude are applied. Histograms of the domain

This article is protected by copyright. All rights reserved.

Author Manuscript

wall depinning field constructed from these images (Figure 4c) indicate depinning fields in the range $0.1 - 0.4$ T (at 5 K), with a decreasing trend with increasing thickness. We note that Reference [29] reported magneto-optical images of a bulk VI_3 crystal during initial magnetization, showing depinning fields of tens of mT, which is even less than for the thick flakes imaged in Figure 4. These values together with the thickness dependence are consistent with cracks extending through a single (or a few) atomic layer (see Supporting Information, section X). Remarkably, however, these defects do not affect the switching process since the corresponding depinning fields are much smaller than H_c, set by the nucleation field.

In summary, we employed widefield NV microscopy to directly reveal the mechanism governing magnetic switching in ultrathin VI_3, a van der Waals magnetic semiconductor. Our images of domain reversal indicate that ultrathin VI_3, down to two atomic layers, is a nucleation-type hard ferromagnet. This is confirmed by images of the initial magnetization revealing domain wall depinning fields far below the switching field. These experiments establish widefield NV microscopy as a powerful tool for magnetic imaging that can be applied to virtually any van der Waals material or heterostructure. By allowing rapid, quantitative imaging of many samples in parallel, it may facilitate the discovery of novel 2D magnetic materials[4,32] and the investigation of magnetic processes including skyrmionics, current-driven domain wall motion and other spintronic phenomena.[33–38]

Author Manuscript

ACKNOWLEDGEMENTS

The authors thank Marcus Doherty and Yuerui Lu for stimulating discussions. The work by the University of Melbourne team was supported by the Australian Research Council (ARC) through grants DE170100129, CE170100012, LE180100037 and DP190101506. B.C.J. acknowledges the AFAiiR node of the NCRIS Heavy Ion Capability for access to ion-implantation facilities. D.A.B. and S.E.L. are supported by an Australian Government Research Training Program Scholarship. The work by the RMIT team was supported by the ARC through grant CE170100039, and was performed in part at the RMIT Micro Nano Research Facility (MNRF) in the Victorian Node of the Australian National Fabrication Facility (ANFF) and the RMIT Microscopy and Microanalysis Facility (RMMF). S.T., C.L. and H.L. are supported by the National Key R&D Program of China (Grants No. 2018YFE0202600, 2016YFA0300504) and the National Natural Science Foundation of

This article is protected by copyright. All rights reserved.

China (Grant No. 11774423, 11822412). Z.W. thanks the computing resources of Tianhe II and the Arcuda super-computer in Skoltech, and acknowledges support by the National Natural Science Foundation of China (Grant No. 11604159).

Author Manuscript

[1] B. Huang, G. Clark, E. Navarro-Moratalla, D. R. Klein, R. Cheng, K. L. Seyler, D. Zhong, E. Schmidgall, M. A. McGuire, D. H. Cobden, W. Yao, D. Xiao, P. Jarillo-Herrero, X. Xu. *Nature* **2017**, *546*, 7657 270.

[2] C. Gong, L. Li, Z. Li, H. Ji, A. Stern, Y. Xia, T. Cao, W. Bao, C. Wang, Y. Wang, Z. Q. Qiu, R. J. Cava, S. G. Louie, J. Xia, X. Zhang. *Nature* **2017**, *546*, 7657 265.

[3] K. Burch, D. Mandrus, J.-G. Park. *Nature* **2018**, *563* 47.

[4] C. Gong, X. Zhang. *Science* **2019**, *363*, 6428 eaav4450.

[5] M. Gibertini, M. Koperski, A. Morpurgo, K. Novoselov. *Nature Nanotechnology* **2019**, *14*, 5 408.

[6] S. Jiang, L. Li, Z. Wang, K. F. Mak, J. Shan. *Nature Nanotechnology* **2018**, *13*, 7 549.

[7] B. Huang, G. Clark, D. R. Klein, D. MacNeill, E. Navarro-Moratalla, K. L. Seyler, N. Wilson, M. A. McGuire, D. H. Cobden, D. Xiao, W. Yao, P. Jarillo-Herrero, X. Xu. *Nature Nanotechnology* **2018**, *13*, 30 544.

[8] T. Li, S. Jiang, N. Sivadas, Z. Wang, Y. Xu, D. Weber, J. Goldberger, K. Watanabe, T. Taniguchi, C. Fennie, K. Mak, J. Shan. *Nature Materials* **2019**, *18* 1303.

[9] W. Chen, Z. Sun, Z. Wang, L. Gu, X. Xu, S. Wu, C. Gao. *Science* **2019**, *366*, 6468 983.

[10] M. A. McGuire, H. Dixit, V. R. Cooper, B. C. Sales. *Chemistry of Materials* **2015**, *27*, 2 612.

[11] B. Chen, J. Yang, H. Wang, M. Imai, H. Ohta, C. Michioka, K. Yoshimura, M. Fang. *Journal of the Physical Society of Japan* **2013**, *82*, 12 124711.

[12] C. Tan, J. Lee, S.-G. Jung, T. Park, S. Albarakati, J. Partridge, M. R. Field, D. G. McCulloch, L. Wang, C. Lee. *Nature Communications* **2018**, *9*, 1 1554.

[13] Z. Fei, B. Huang, P. Malinowski, W. Wang, T. Song, J. Sanchez, W. Yao, D. Xiao, X. Zhu, A. F. May, W. Wu, D. H. Cobden, J.-H. Chu, X. Xu. *Nature Materials* **2018**, *17*, 9 778.

[14] Y. Deng, Y. Yu, Y. Song, J. Zhang, N. Wang, Y. Wu, J. Zhu, J. Wang, X. Chen, Y. Zhang. *Nature* **2018**, *563* 94.

This article is protected by copyright. All rights reserved.

Author Manuscript

[15] S. Steinert, F. Dolde, P. Neumann, A. Aird, B. Naydenov, G. Balasubramanian, F. Jelezko, J. Wrachtrup. *Rev. Sci. Instrum.* **2010**, *81*, 4 043705.

[16] D. Le Sage, K. Arai, D. R. Glenn, S. J. DeVience, L. M. Pham, L. Rahn-Lee, M. D. Lukin, A. Yacoby, A. Komeili, R. L. Walsworth. *Nature* **2013**, *496*, 7446 486.

[17] D. A. Simpson, J. P. Tetienne, J. M. McCoey, K. Ganesan, L. T. Hall, S. Petrou, R. E. Scholten, L. C. Hollenberg. *Sci. Rep.* **2016**, *6*, October 2015 22797.

[18] J.-P. Tetienne, N. Dontschuk, D. A. Broadway, A. Stacey, D. A. Simpson, L. C. L. Hollenberg. *Sci. Adv.* **2017**, *3*, 4 e1602429.

[19] P. Maletinsky, S. Hong, M. Grinolds, B. Hausmann, M. Lukin, R. Walsworth, M. Loncar, A. Yacoby. *Nature Nanotechnology* **2012**, *7*, 5 320324.

[20] J.-P. Tetienne, T. Hingant, J.-V. Kim, L. H. Diez, J.-P. Adam, K. Garcia, J.-F. Roch, S. Rohart, A. Thiaville, D. Ravelosona, V. Jacques. *Science* **2014**, *344*, 6190 1366.

[21] L. Thiel, Z. Wang, M. A. Tschudin, D. Rohner, I. Gutiérrez-Lezama, N. Ubrig, M. Gibertini, E. Giannini, A. F. Morpurgo, P. Maletinsky. *Science* **2019**, *364* 973976.

[22] J.-P. Tetienne, D. A. Broadway, S. E. Lillie, N. Dontschuk, T. Teraji, L. T. Hall, A. Stacey, D. A. Simpson, L. C. L. Hollenberg. *Sensors* **2018**, *18* 1290.

[23] M. W. Doherty, N. B. Manson, P. Delaney, F. Jelezko, J. Wrachtrup, L. C. L. Hollenberg. *Physics Reports* **2013**, *528*, 1 1.

[24] L. Rondin, J. P. Tetienne, T. Hingant, J. F. Roch, P. Maletinsky, V. Jacques. *Rep. Prog. Phys.* **2014**, *77*, 5 56503.

[25] F. Casola, T. Van Der Sar, A. Yacoby. *Nature Reviews Materials* **2018**, *3* 17088.

[26] S. E. Lillie, D. A. Broadway, N. Dontschuk, S. C. Scholten, B. C. Johnson, S. Wolf, S. Rachel, L. C. L. Hollenberg, J.-P. Tetienne. *Nano Letters* **2020**, *20*, 3 1855.

[27] S. Tian, J.-F. Zhang, C. Li, T. Ying, S. Li, X. Zhang, K. Liu, H. Lei. *Journal of the American Chemical Society* **2019**, *141*, 13 5326.

[28] S. Son, M. J. Coak, N. Lee, J. Kim, T. Y. Kim, H. Hamidov, H. Cho, C. Liu, D. M. Jarvis, P. A. C. Brown, J. H. Kim, C.-H. Park, D. I. Khomskii, S. S. Saxena, J.-G. Park. *Phys. Rev. B* **2019**, *99* 041402.

[29] T. Kong, K. Stolze, E. I. Timmons, J. Tao, D. Ni, S. Guo, Z. Yang, R. Prozorov, R. J. Cava. *Advanced Materials* **2019**, *31*, 17 1808074.

[30] J. M. D. Coey. *Magnetism and Magnetic Materials*. Cambridge University Press, **2010**.

This article is protected by copyright. All rights reserved.

Author Manuscript

[31] J. Yan, X. Luo, F. C. Chen, J. J. Gao, Z. Z. Jiang, G. C. Zhao, Y. Sun, H. Y. Lv, S. J. Tian, Q. W. Yin, H. C. Lei, W. J. Lu, P. Tong, W. H. Song, X. B. Zhu, Y. P. Sun. *Phys. Rev. B* **2019**, *100* 094402.

[32] N. Mounet, M. Gibertini, P. Schwaller, D. Campi, A. Merkys, A. Marrazzo, T. Sohier, I. E. Castelli, A. Cepellotti, G. Pizzi, N. Marzari. *Nature Nanotechnology* **2018**, *13* 246.

[33] A. Fert, V. Cros, J. Sampaio. *Nature Nanotechnology* **2013**, *8*, 3 152.

[34] S. Emori, U. Bauer, S.-M. Ahn, E. Martinez, G. Beach. *Nature Materials* **2013**, *12* 611.

[35] K. L. W. Xiaoyang Lin, Wei Yang, W. Zhao. *Nature Electronics* **2019**, *2* 274.

[36] S. Shi, S. Liang, Z. Zhu, K. Cai, S. Pollard, Y. Wang, J. Wang, Q. Wang, P. He, J. Yu, G. Eda, G. Liang, H. Yang. *Nature Nanotechnology* **2019**, *14* 945.

[37] M.-G. Han, J. A. Garlow, Y. Liu, H. Zhang, J. Li, D. DiMarzio, M. W. Knight, C. Petrovic, D. Jariwala, Y. Zhu. *Nano Letters* **2019**, *19*, 11 7859.

[38] B. Ding, Z. Li, G. Xu, H. Li, Z. Hou, E. Liu, X. Xi, F. Xu, Y. Yao, W. Wang. *Nano Letters* **2020**, *20*, 2 868.

This article is protected by copyright. All rights reserved.